Nanoscale

Accepted Manuscript

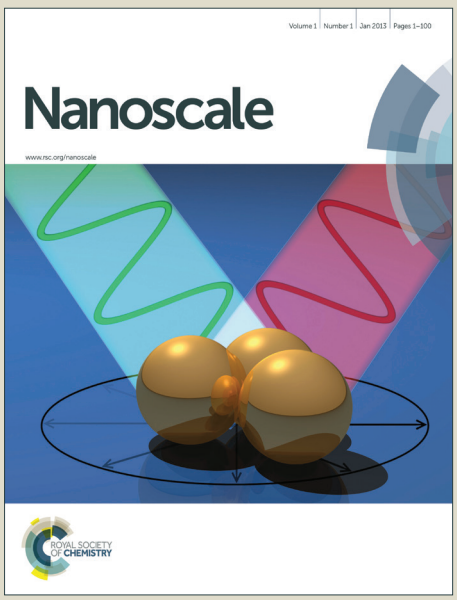

ROYAL SOCIETY OF CHEMISTRY

www.rsc.org/nanoscale

Nanoscale

RSCPublishing

COMMUNICATION

Bottom-up nanostructured bulk silicon: A practical high-efficiency thermoelectric material

Cite this: DOI: 10.1039/x0xx00000x

Aikebaier Yusufu,[a] Ken Kurosaki,*[a] Yoshinobu Miyazaki,[a] Manabu Ishimaru,[b] Atsuko Kosuga,[c] Yuji Ohishi,[a] Hiroaki Muta,[a] and Shinsuke Yamanaka,[a,d]

Received 00th January 2012,
Accepted 00th January 2012

DOI: 10.1039/x0xx00000x

www.rsc.org/

The effectiveness of Thermoelectric (TE) materials is quantified by the dimensionless figure of merit (zT). An ideal way to enhance zT is by scattering phonons without scattering electrons. Here we show that, using a simple bottom-up method, we can prepare bulk nanostructured Si that exhibits exceptionally high zT of 0.6 at 1050 K, at least three times higher than that of optimized bulk Si. The nanoscale precipitates in this material connected coherently or semi-coherently with the Si matrix, effectively scattering heat-carrying phonons without significantly influencing the material's electron transport properties, leading to the high zT.

Introduction

The energy demands of economic and social development are continually rising. However, over 60% of primary energy is exhausted as waste heat,[1] necessitating efficient re-use of waste heat. Thermoelectrics (TEs) can generate electricity from a temperature difference according to the Seebeck effect; inversely, applying an electrical current generates a temperature difference according to the Peltier effect. These effects can be respectively used to generate power from waste heat and for solid-state refrigeration.[2-4] However, current TE devices have low efficiency, limiting their applications in power generation to niche areas such as in NASA spacecraft.[5] Extensive industrial applications, such as generating power from exhaust heat in automobiles, have not been achieved.

The efficiency of a TE device depends on the properties of the TE material used and the temperature difference applied across the device. The effectiveness of a TE material is represented by the dimensionless figure of merit, $zT = (S^2\sigma)T/(\kappa_{el}+\kappa_{lat})$, where S, σ, T, κ_{el}, and κ_{lat} are the Seebeck coefficient, electrical conductivity, absolute temperature, and electronic and lattice components of the thermal conductivity, respectively.[6] S, σ, and κ_{el} depend on the carrier density of the material, meaning that zT can be effectively increased by decreasing κ_{lat}. The best materials currently used in TE devices are PbTe-based materials for power generation at high temperatures[5] and Bi_2Te_3-based materials for refrigeration near room temperature.[7] The zT values of these conventional materials are ≈1, corresponding to device efficiencies of several percent. Along with their inadequate efficiency, these conventional materials contain highly toxic and/or rare elements such as Bi, Te, and Pb. Thus, many desire to develop high-efficiency TE materials made from elements that are less expensive, more Earth-abundant, and more environmentally friendly.

Si is a non-toxic, inexpensive, and naturally abundant element. Although bulk Si exhibits good electrical properties (i.e., high $S^2\sigma$), its κ_{lat} is high (>100 $Wm^{-1}K^{-1}$), leading to a zT of ≈0.01 at room temperature.[8] If its κ_{lat} could be lowered while maintaining high $S^2\sigma$, Si could be an ideal TE material. These changes can be realized in Si by nanostructuring.[7, 9-16]

Bulk nanostructured TE materials are typically made in one of two ways: forming a bulk by fabricating and consolidating fine nanocrystals (top-down process) or forming a bulk by precipitating nanoscale particles (bottom-up process). These top-down structures are commonly prepared by using ball milling (BM) followed by hot pressing (HP) or spark plasma sintering (SPS). Top-down methods are effective and have been used to prepare various conventional TE materials, including $Bi_xSb_{2-x}Te_3$[7] and Si–Ge[14, 15] alloys. Top-down *p*-type $Bi_xSb_{2-x}Te_3$ bulk nanocrystals have exhibited a maximum zT of 1.4,[7] compared to a peak zT of ≈1 for conventional bulk materials. However, top-down methods have some drawbacks: undesirable impurities may be incorporated during BM, nanocrystals may grow too much during HP/SPS, and oxidization may be difficult to avoid during BM and/or HP/SPS.

Bottom-up materials are usually prepared by solidifying a melt under appropriate cooling conditions. Bottom-up SrTe–PbTe materials, in which nanoscale SrTe is naturally precipitated in the PbTe matrix, have exhibited record-high zT of ≈2.2.[16] However, bottom-up methods have been realized almost in lead chalcogenides such as PbS[17], PbSe,[17, 18] and PbTe.[17, 19]

Because Si nanopowders oxidize easily, it is difficult to apply the BM-HP/SPS method to create bulk nanostructured Si. The Si–Ge nanocrystals reported so far have been prepared under carefully controlled atmospheres, such as in an Ar-filled globe box.[14, 15] In the

present study, we successfully prepared bulk nanostructured Si using an easy, reliable bottom-up method, by arc melting super-heavily P-doped Si, crushing it into micropowder, and then performing SPS in desirable conditions. Two kinds of nanoscale precipitates naturally formed in the grains of the polycrystalline Si matrix: semi-coherent plate-like P-rich precipitates with sizes of a few dozen nanometres, and coherent spherical precipitates with diameters of several nanometres Fig. 1a. These nanoscale precipitates effectively scattered the heat-carrying phonons without significantly influencing the material's electron transport properties, greatly decreasing κ_{lat} and leading to a zT of 0.6 at 1050 K, at least three times higher than that of optimized bulk Si Fig. 1b.

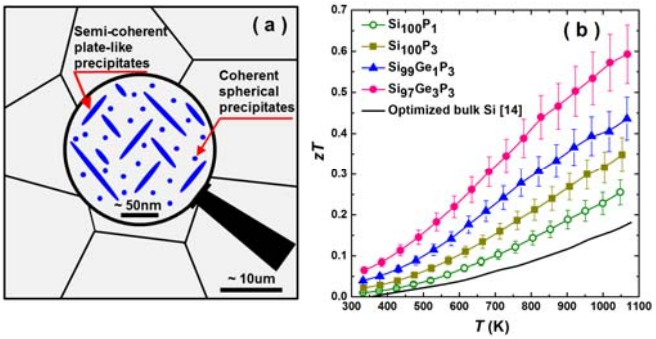

Fig. 1 (a) Micro- and nanoscale schematics of nanostructured bulk Si prepared in the present study. The polycrystalline bulk Si, whose grain size ranged from several micrometres to a few dozen micrometres, contained two kinds of naturally formed nanoscale precipitates: semi-coherent plate-like P-rich precipitates with sizes ranging from a few dozen nanometres and coherent spherical precipitates with sizes of several nanometres. (b) Temperature dependence of zT in nanostructured bulk Si with an uncertainly of 12%.

In the Si–P phase diagram[20] (see Fig. S1 in the Supplementary Information), the solubility of P in Si depends much on temperature: the solubility limit is ≈2.4 at.% at 1453 K and almost zero at room temperature. This phase diagram suggests that a P-rich phase will precipitate when solidifying super-heavily P-doped Si from a melt. To investigate how Ge influences precipitation and to introduce phonon-scattering centres to decrease κ_{lat}, we added very small amounts of Ge to the super-heavily P-doped Si. According to this conception, in the present report we studied compositions of $Si_{100}P_1$, $Si_{100}P_3$, $Si_{99}Ge_1P_3$, and $Si_{97}Ge_3P_3$.

Results and Discussion

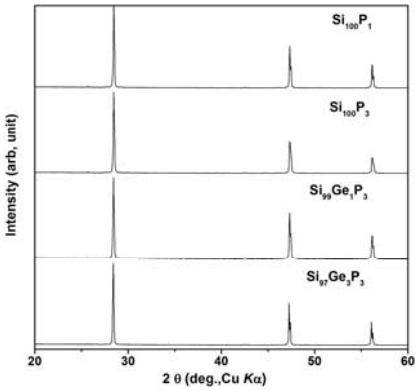

Fig. 2 Powder XRD patterns, produced by crushing parts of the sintered pellets prepared by SPS.

As shown in Fig. 2 the powder XRD patterns of the present samples exhibited very sharp peaks corresponding to Si with no impurity peaks, revealing them to be single-phase materials. Table 1 summarizes the lattice parameters (a) calculated from these XRD patterns. The a of $Si_{100}P_1$ and $Si_{100}P_3$ were smaller than that of pure Si (a = 0.5431nm),[21] and $Si_{100}P_3$ exhibited a slightly smaller a than $Si_{100}P_1$. Adding Ge (i.e., $Si_{99}Ge_1P_3$ and $Si_{97}Ge_3P_3$) increased a with increasing Ge content. We attribute these results to the atomic radius of P (0.110 nm)[22] being slightly smaller than that of Si (0.117 nm)[22] and because substituting Ge for Si increased the a of Si. SEM images (see Fig. S2 in the Supplementary Information) revealed that all samples were dense with no remarkable cracks and pores and that their grain sizes ranged from several micrometres to a few dozen micrometres. Quantitative EDX analyses revealed that Ge was uniformly distributed in the samples and that their contents were nearly the same as their starting compositions. However, we could not obtain accurate P contents because it was within the error range of EDX. Table 1 summarizes the bulk densities of the samples, revealing that the sample densities were high enough (≈98% of theoretical density) for TE characterization.

Table 1 lists the n_H and μ_H of the samples, calculated from measured room-temperature R_H. All samples exhibited very high n_H, on the order of 10^{20} cm^{-3}. For $Si_{100}P_1$ and $Si_{100}P_3$, n_H increased with increasing P content because P-doping supplied electrons to Si. For $Si_{100}P_3$, $Si_{99}Ge_1P_3$, and $Si_{97}Ge_3P_3$, the n_H decreased with increasing Ge content, despite their having the same P content as their starting

Table I Lattice parameter a, density d, Hall carrier concentration n_H (300 K), Hall mobility μ_H (300 K), Seebeck coefficient S (300 K), electrical conductivity σ (300 K), lattice thermal conductivity κ_{lat} (300 K), and maximum zT_{max} (1070 K) of $Si_{100}P_1$, $Si_{100}P_3$, $Si_{99}Ge_1P_3$, and $Si_{97}Ge_3P_3$.

	a nm	d g cm^{-1}	%TD	n_H 10^{20} cm^{-3}	μ_H cm^2 V^{-1} s^{-1}	S μV K^{-1}	σ 10^5 S m^{-1}	κ_{lat} Wm^{-1}K^{-1}	zT_{max} -
$Si_{100}P_1$	0.54238	2.30	98	1.82	56	-77	1.85	42	0.26
$Si_{100}P_3$	0.54237	2.30	98	3.84	43	-77	2.52	25	0.35
$Si_{99}Ge_1P_3$	0.54243	2.35	98	3.54	45	-75	2.31	12	0.44
$Si_{97}Ge_3P_3$	0.54343	2.40	98	2.09	53	-87	2.12	9	0.60

compositions. This behaviour was caused by pure Si having higher P-solubility than Si–Ge alloys; the solubility limit of P is 2.4 at.% at 1453 K for pure Si[20] and 1.8 at.% at 1050 K for a $Si_{80}Ge_{20}$ alloy.[23] We also confirmed that samples with larger n_H had smaller μ_H.

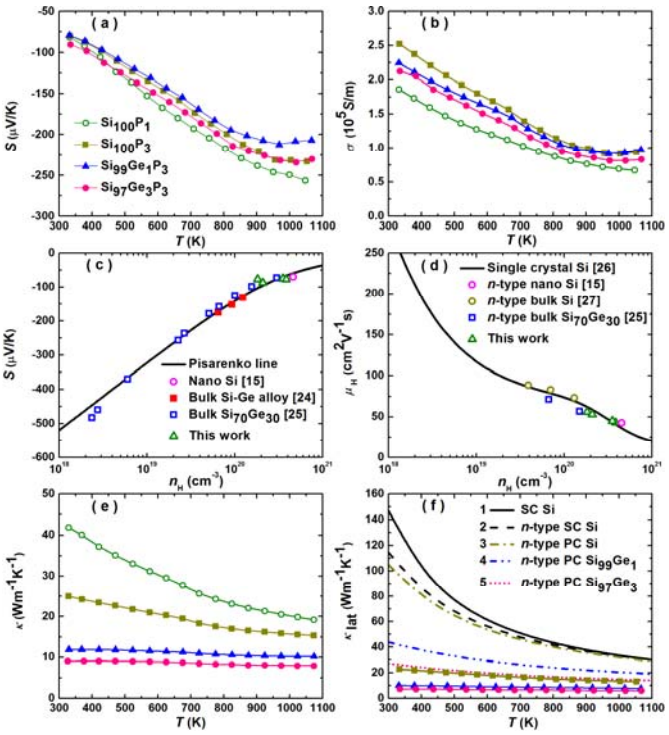

Fig. 3 Temperature dependences of (a) Seebeck coefficient S and (b) electrical conductivity σ of nanostructured bulk Si. Also shown are relationships between (c) S and the carrier concentration n_H and (d) carrier mobility μ_H at room temperature. In (c), the theoretical Pisarenko line is shown for comparison. Also shown are the temperature dependences of (e) thermal conductivity κ and (f) lattice thermal conductivity κ_{lat} of nanostructured bulk Si. In (e), lines calculated from the Born–von Karman dispersion model are shown; lines 1, 2, 3, 4, and 5 represent the calculated results for non-doped single crystal (SC) Si, heavily-doped SC Si (3×10^{20} cm^{-3}), heavily-doped polycrystalline (PC) Si (3×10^{20} cm^{-3}, grain size: 5 μm), heavily-doped PC Si containing 1 at.% Ge (3×10^{20} cm^{-3}, grain size: 5 μm), and heavily-doped PC Si containing 3 at.% Ge (3×10^{20} cm^{-3}, grain size: 5 μm), respectively.

Fig. 3(a) and (b) show how S and σ depended on temperature, respectively. Fig. 3(a) reveals that all samples exhibited negative S, indicating the samples were n-type and the majority carriers were electrons. As the temperature increased, the absolute value of S increased while σ decreased, typical behaviour of degenerate semiconductors. These tendencies agree well with previous data for Si-based TE materials.[14, 15] Above ≈900 K, the temperature dependency of the absolute values of S and σ tended to change, likely related to the increased carrier concentration caused by the increased solubility limit of P for Si at high temperatures. We could not confirm a clear relationship between S and n_H. To examine the electrical transport properties of the samples, we plot the room-temperature S and μ_H as functions of n_H in Fig. 3(c) and (d), respectively, showing previous data[15, 24-27] for Si-based TE materials for comparison. Fig. 3(c) shows the theoretical Pisarenko line, calculated by using Eqs. (1), (2), and (3). The S of the single-parabolic-band model can be expressed as

$$S = \frac{k_B}{e}\left[\eta - \frac{(2+\lambda)F_{(1+\lambda)}(\eta)}{(1+\lambda)F_{\lambda}(\eta)}\right], \quad (1)$$

$$n_H = 4\pi\left(\frac{2m^* k_B T}{h^2}\right)^{3/2} F_{1/2}(\eta), \quad (2)$$

$$F(\eta) = \int_0^{\infty} \frac{x^{\lambda} dx}{1+\exp(x-\eta)}, \quad (3)$$

where η, m^*, k_B, h, $F(\eta)$, and λ are the reduced Fermi level (= E_F/k_BT, where E_F is the Fermi level), carrier effective mass (= $1.08m_0$,[28] where m_0 is the free electron mass), Boltzmann constant, Planck constant, Fermi integral, and scattering parameter, respectively. λ is a parameter that explains the energy dependence of the charge-carrier mean free path; λ = 0, 1, and 2 correspond to both acoustic phonon scattering and alloy disorder scattering, optical phonon scattering, and ionized impurity scattering, respectively.[29] In the present study, we obtained λ = 0.65 by fitting the literature data,[15, 24, 25] a reasonable result because it has been reported that λ = 0–1 gives a good fit to experimental S values for Si–Ge alloys.[30] Examining Fig. 3 (c), we confirm that our data exist on the theoretical Pisarenko line. Also, Fig. 3 (d) shows that the relationship between n_H and μ_H for our data almost matched those from the literature data of Si-based TE materials.[15, 25-27] These results indicate that the electrical transport properties of our samples are similar to those of traditional Si-based bulk TE materials.

Fig. 3(e) shows how κ depended on temperature. All samples exhibited low κ, decreasing with increasing P and Ge contents. $Si_{97}Ge_3P_3$ exhibited the lowest κ, <10 Wm^{-1}K^{-1} over the entire temperature range. To understand the phonon transport properties of the samples, we calculated and analysed κ_{lat}, as shown in Fig. 3(f). In this figure, lines 1, 2, 3, 4, and 5 represent the calculated data for non-doped single crystal Si, heavily-doped single crystal Si (3×10^{20} cm^{-3}), heavily-doped polycrystalline Si (3×10^{20} cm^{-3}, grain size: 5 μm), heavily-doped polycrystalline Si containing 1 at.% Ge (3×10^{20} cm^{-3}, grain size: 5 μm), and heavily-doped polycrystalline Si containing 3 at.% Ge (3×10^{20} cm^{-3}, grain size: 5 μm), respectively. These lines were obtained from theoretical calculations using a Born–von Karman dispersion model that included frequency-dependent expressions for grain-boundary scattering.[31] In this model, κ_{lat} can be expressed as:

$$\kappa_{lat} = \sum_p \frac{1}{3}\int C \cdot \upsilon^2 \cdot \tau_c \cdot d\omega, \quad (4)$$

where C, υ, τ_c, and ω are the specific heat capacity, group velocity, relaxation time, and frequency, respectively. When calculating κ_{lat}, we considered four kinds of phonon scattering: Umklapp scattering, phonon-impurity scattering, grain-boundary phonon scattering, and phonon-electron scattering. Thus, we estimated the τ_c as follows:

$$\tau_c^{-1}(\omega,T) = \tau_{umkl}^{-1}(\omega,T) + \tau_{imp}^{-1}(\omega) + \tau_{bdy}^{-1}(\omega) + \tau_{ep}^{-1}(\omega,T), \quad (5)$$

where τ_{umkl}, τ_{imp}, τ_{bdy}, and τ_{ep} are the relaxation times determined by Umklapp scattering, phonon-impurity scattering, grain-boundary

phonon scattering, and phonon-electron scattering. Each scattering parameter can be written as summarized in Table S1.

In this model, we considered four kinds of phonon scattering: Umklapp scattering, phonon-impurity scattering, grain-boundary phonon scattering, and phonon-electron scattering. The theoretical lines for non-doped (line 1) and heavily-doped (line 2) single crystal Si agree well with previous experimental data.[14, 15] Comparing lines 1 and 2, we confirm that P doping of Si reduced κ_{lat} by influencing both phonon-impurity and phonon-electron scattering. Comparing lines 2 and 3, we confirm that polycrystalline Si with a grain size of 5 μm had slightly low κ_{lat} than that of single crystal Si because of grain-boundary phonon scattering. Comparing lines 3, 4, and 5, we confirm that substituting Ge for Si significantly reduced κ_{lat} by increasing phonon-impurity scattering, even at low Ge content of 1–3 at.%. As described previously, the grain sizes of our samples ranged from several micrometres to a few dozen micrometres (see Fig. S2 in the Supplementary Information) and exhibited n_H values around 3×10^{20} cm^{-3} (see Table 1). Thus, the experimentally determined κ_{lat} of $Si_{100}P_3$, $Si_{99}Ge_1P_3$, and $Si_{97}Ge_3P_3$ should agree with the theoretically calculated lines of 3, 4, and 5, respectively. However, as shown in Fig. 3(f), the experimental κ_{lat} were significantly lower than those of the theoretical lines. To understand this difference, we carefully observed the microstructures of the samples by using TEM.

Fig. 4 shows the TEM microstructure of a bulk $Si_{99}Ge_1P_3$ sample. The grain size in this sample was much larger than the image dimensions, so these images were mainly used to identify defects within a single grain. A bright-field (BF) image at low magnification (Fig. 4(a)) shows a high density of precipitates dispersed in a matrix as well as dark contrast around the precipitates, caused by strain. Because the precipitate density and size varied widely in each grain, quantitative analysis is difficult. We found similar precipitates in $S_{100}P_1$, $Si_{100}P_3$, and $Si_{97}Ge_3P_3$ (see Fig. S4 in the Supplementary Information). In these samples, the form and density of the precipitates appeared to be the same. However, the samples with less P had obviously smaller precipitate density.

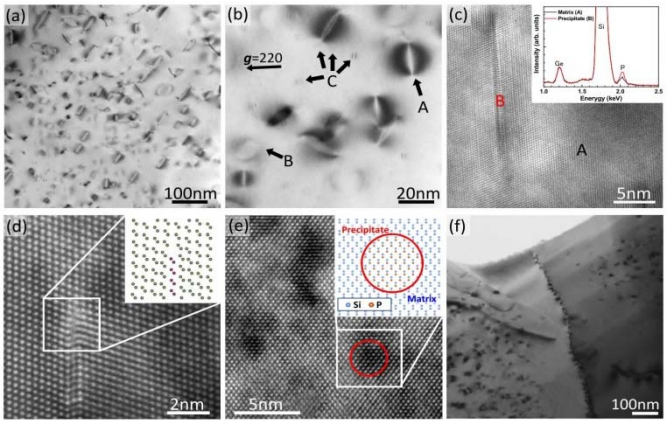

Fig. 4 TEM of the microstructure of a bulk $Si_{99}Ge_1P_3$ sample. (a) Low- and (b) high-magnification bright-field images, showing contrast from stain around the precipitates; (c) HRTEM and EDS of a plate-like precipitate; HRTEM lattice image and structural model of (d) a plate-like precipitate taken along the [110] direction and (e) nearly spherical precipitates; a (f) low-magnification bright-field image showing a grain boundary.

The higher-magnification BF image in Fig. 4(b) shows two types of precipitates, both in morphology and size. One is a plate-like precipitate with a diameter of 15–100 nm. As indicated by arrow A, this type of precipitate exhibited high contrast, likely caused by misfit strain. As shown by arrow B, we also observed areas of lesser contrast. These differing contrasts were likely caused by the differences in the directions of the plate-like precipitates: that is, the high contrast occurred for precipitates along the incident direction of the electron beam, while the lesser contrast occurred for precipitates nearly perpendicular to the incident direction of electron beam. Similar precipitates and contrast have been observed in some metals.[32] Most plate-like precipitates were embedded in the Si matrix parallel to the {111} plane. Aside from these, we observed very small (<5 nm) precipitates with butterfly-like shade, indicated by the C arrows, all parallel to the (110) plane. We believe the small precipitates exhibited Ashby–Brown's contrast[33, 34] caused by the strain field around the nearly spherical coherent precipitates.

As shown in Fig. 4(c), EDS point-analysis revealed that the plate-like precipitate at point B contained more P than the Si matrix at point A, while there was no difference in Ge content. Unfortunately, quantitative EDS analysis of chemical composition was difficult because we could not focus the electron beam only on the precipitate. Fig. 4(d) shows a lattice image and atomic-structure model of the end of a plate-like precipitate viewed along the [110] direction, revealing an edge dislocation at the end of the precipitate and an extra single lattice plane in the precipitate. The lattice image and the structural model of another precipitate viewed along the [211] direction are shown in Fig. S4(d) in the Supplementary Information. From these results, we conclude that the plate-like precipitates are a P-rich compound and connect semi-coherently with the Si matrix.

In contrast, the lattice image in Fig. 4(e) shows dark spots corresponding to the very small spherical precipitates. Because this lattice pattern matches that of the Si matrix, we conclude that the very small precipitates connected coherently with the Si matrix. Although quantitative EDS analysis was impossible because the precipitates were too small, we adopted a model of a diamond cubic structure with P substituting in half of the Si sites, as shown in Fig. 4(e). Such SiP precipitates with this cubic structure have been found in P-supersaturated Si,[35] and a simulated model[36] agrees with our observations. Generally, the crystal system of SiP is not cubic but orthorhombic, meaning bulk cubic SiP is not thermodynamically stable. However, the interface energy becomes more dominant as the precipitate size decreases, making cubic SiP stable when it exists as nanoscale precipitates in the Si matrix.

The precipitate size decreased near the grain boundaries, leading to areas where no precipitates formed, as shown in Fig. 4(f) and Fig. S4(e) in the Supplementary Information. We believe that the nanoscale precipitates form by following these four steps: (1) super-heavily P-doped Si crystallizes at a high temperature; (2) the solubility limit of P into Si decreases with decreasing temperature; (3) excess P leaves the Si matrix; and (4) nanoscale P-rich phases naturally precipitate. Near the grain boundaries, the excess P seems to be driven out to the grain boundaries. The presence of this area lacking precipitates near the grain boundaries indicates that a sufficiently large grain size (more than several micrometres) is required to precipitate large amounts of P-rich nanoscale particles.

Conclusions

The polycrystalline $Si_{97}Ge_3P_3$ exhibited a significantly higher zT of 0.6, more than three times that of optimized bulk Si, as shown in Fig. 1(b). The most important way to maintain high $S^2\sigma$ in the nanostructure is to ensure that the precipitates coherently or semi-coherently connect with the Si matrix. In the PbTe system,[17] electrons are rarely scattered by such perfect interfacial surfaces, but phonons are scattered. This is an ideal situation for TE materials and the same situation realizes in the present case. In fact, the nanoscale precipitates in the present samples do not strongly influence either S or μ_H but significantly decrease κ_{lat}, as shown in Fig. 3(c), (d), and (f). The size and distribution of the nanoscale precipitates could be controlled by adjusting the P and Ge contents, allowing for further enhancement of zT. Because Si has many advantageous in cost and toxicity compared to Bi, Te, and Pd, used in conventional TE materials, the nanostructured bulk Si prepared in the present study is a promising and scalable TE material.

Experimental

The starting materials—Si chunks (11N), Ge shots (5N), and P chunks (4N)—were weighed and mixed to the desired compositions and melted by arc melting in an Ar atmosphere. The ingots produced by arc melting were then crushed into micropowders, which were placed in a graphite die for SPS at 1353 K for 3 min under an axial pressure of 100 MPa in an Ar atmosphere. The bulk samples produced by SPS were characterized using powder X-ray diffraction (XRD; Rigaku RINT2000) with Cu-Kα radiation at room temperature. The microstructure and chemical composition of the samples were studied by using scanning electron microscopy (SEM; Hitachi S-2600H) and energy-dispersive X-ray spectroscopy (EDX; Horiba EX-200). The density (d) of each bulk sample was calculated based on its measured weight and dimensions.

Microstructures were characterized by transmission electron microscopy (TEM). For each TEM observation, each thin specimen was prepared by crushing the bulk sample into powder, and then collecting the powders on a perforated amorphous carbon film supported by a copper grid. TEM was performed at an accelerating voltage of 200 kV in bright-field (BF) mode (Hitachi H800), using high-resolution transmission electron microscopy (HRTEM; JEOL 2100), and using HRTEM (JEOL ARM200F) equipped with a silicon drift detector in combination with an ultrahigh-sensitivity energy dispersive X-ray spectroscopy (EDS) instrument.

σ and S were measured simultaneously in a He atmosphere at 323–1073 K (Ulvac ZEM-3). The Hall coefficient (R_H) was measured (Toyo Resitest8300) at room temperature by the van der Pauw method in vacuum under an applied magnetic field of 0.5 T. The Hall carrier concentration (n_H) and Hall mobility (μ_H) were calculated from R_H based by assuming a single-band model and a Hall factor of 1; i.e., $n_H = 1/(eR_H)$ and $\mu_H = \sigma R_H$, where e is the elementary electric charge. κ was evaluated from the thermal diffusivity (α), heat capacity (C_p), and d by $\kappa = \alpha C_p d$. α was measured at 323–1073 K by the laser flash diffusivity method (Netzsch LFA-457). C_p data of pure Si were used to calculate the κ for all samples. The validity of this calculation was checked by measuring the low-temperature C_P of $Si_{97}Ge_3P_3$ using a Physical Property Measurement System (PPMS; Quantum Design). As shown in Fig. S3 in the Supplementary Information, the measured C_P was well consistent with the C_P of $Si_{97}Ge_3P_3$ estimated based on the Kopp-Neumann rule and slightly lower than the C_P of pure Si.[37] This tendency will continue even at high temperatures. Thus, we decided that the C_P of pure Si can be used instead of those of Si containing a small amount of Ge (in this case, 3 at.% maximum). σ, S, and α data were each measured a few times; these data have measurement errors of ≈3%, resulting in zT uncertainty of ≈12%.

Acknowledgements

This work was supported in part by a Grant-in-Aid for Scientific Research (No. 25289220) from the Ministry of Education, Culture, Sports, Science and Technology of Japan (MEXT). This work was also supported by the ALCA (Advanced Low Carbon Technology Research and Development Program) of the Japan Science and Technology Agency. A part of this work was conducted at the Ultramicroscopy Research Center, Kyushu University, supported by the Nanotechnology Platform Program (Advanced Characterization Nanotechnology Platform) of MEXT, and we appreciate Dr. Y. Shimada for his operation of JEOL ARM200F TEM. TEM observations were also performed using facilities of the Research Center for Ultra-High Voltage Electron Microscopy Osaka University, and the Institute for Solid State Physics, the University of Tokyo.

Notes and references

[a]Graduate School of Engineering, Osaka University, Suita 565-0871, Japan.
[b]Graduate School of Engineering, Kyushu Institute of Technology, Fukuoka 804-8550, Japan.
[c]Nanoscience and Nanotechnology Research Center, Osaka Prefecture University, Osaka 599-8570, Japan.
[d]Research Institute of Nuclear Engineering, University of Fukui, Tsuruga 914-0055, Japan.

†Electronic Supplementary Information (ESI) available: [details of any supplementary information available should be included here].

References

1. T. Kajikawa, *in Thermoelectrics Handbook: Macro to Nano*, ed. D. M. Rowe, CRC/Taylor & Francis, Boca Raton, 2006., ch. 50, pp.50-1.
2. H. J. Goldsmid, *Thermoelectric Refrigeration*, Plenum Press, New York, 1964.
3. G. G. Yadav, J. A. Susoreny, G. Zhang, H. Yang and Y. Wu, *Nanoscale*, 2011, **3**, 3555.
4. L. E. Bell, *Science*, 2008, **321**, 1457-1461.
5. J. Yang and T. Caillat, *MRS Bull.*, 2006, **31**, 224.
6. G. J. Snyder and E. S. Toberer, *Nat. Mater.*, 2008, **7**, 105.
7. B. Poudel, Q. Hao, Y. Ma, Y. Lan, A. Minnich, B. Yu, X. Yan, D. Wang, A. Muto, D. Vashaee, X. Chen, J. Liu, M. S. Dresselhaus, G. Chen and Z. Ren, *Science*, 2008, **320**, 634-638.
8. L. Weber and E. Gmelin, *Appl. Phys. A*, 1991, **53**, 136.
9. M. S. Dresselhaus, G. Chen, M. Y. Tang, R. G. Yang, H. Lee, D. Z. Wang, Z. F. Ren, J. P. Fleurial and P. Gogna, *Adv. Mater.*, 2007, **19**, 1043.
10. R. Venkatasubramanian, E. Siivola, T. Colpitts and B. O'Quinn, *Nature*, 2001, **413**, 597.
11. A. I. Hochbaum, R. Chen, R. D. Delgado, W. Liang, E. C. Garnett, M. Najarian, A. Majumdar and P. Yang, *Nature*, 2008, **451**, 163-167.
12. A. I. Boukai, Y. Bunimovich, J. Tahir-Kheli, J. K. Yu, W. A. Goddard and J. R. Heath, *Nature*, 2008, **451**, 168-171.

13. J. Tang, H. T. Wang, D. H. Lee, M. Fardy, Z. Huo, T. P. Russell and P. Yang, *Nano Lett.*, 2010, **10**, 4279-4283.
14. G. Zhu, H. Lee, Y. Lan, X. Wang, G. Joshi, D. Wang, J. Yang, D. Vashaee, H. Guilbert, A. Pillitteri, M. Dresselhaus, G. Chen and Z. Ren, *Phys. Rev. Lett.*, 2009, **102**, 196803.
15. S. K. Bux, R. G. Blair, P. K. Gogna, H. Lee, G. Chen, M. S. Dresselhaus, R. B. Kaner and J.-P. Fleurial, *Adv. Funct. Mater.*, 2009, **19**, 2445-2452.
16. K. Biswas, J. He, I. D. Blum, C. I. Wu, T. P. Hogan, D. N. Seidman, V. P. Dravid and M. G. Kanatzidis, *Nature*, 2012, **489**, 414-418.
17. L.-D. Zhao, V. P. Dravid and M. G. Kanatzidis, *Energy Environ. Sci.*, 2014, **7**, 251.
18. Y. Lee, S. H. Lo, J. Androulakis, C. I. Wu, L. D. Zhao, D. Y. Chung, T. P. Hogan, V. P. Dravid and M. G. Kanatzidis, *J. Am. Chem. Soc.*, 2013, **135**, 5152-5160.
19. Y. Pei, N. A. Heinz, A. LaLonde and G. J. Snyder, *Energy Environ. Sci.*, 2011, **4**, 3640.
20. R. W. Olesinski, N. Kanani and G. J. Abbaschian, *Bull. Alloy Phase Diagrams*, 1985, **6**, 130.
21. J. P. Dismukes, L. Ekstrom and R. J. Pfaff, *J. Phys. Chem. Solids.*, 1964, **68**, 3021.
22. C. Kittel, *Introduction to Solid State Physics*, Wiley, New York, 1966.
23. F. D. Rosi, *Solid-State Electron.*, 1968, **11**, 833.
24. O. A. Golikova, E. K. Iordanishvili, A. V. Petrov and F. T. Tela, *Sov. Phys. Solid State*, 1966, **8**, 397.
25. J. P. Dismukes, L. Ekstrom, E. F. Steigmeier, I. Kudman and D. S. Beers, *J. Appl. Phys.*, 1964, **35**, 2899.
26. G. Masetti, M. Severi and S. Solmi, *IEEE Trans. Elecron Devices*, 1983, **30**, 764.
27. F. Morin and J. Maita, *Phys. Rev.*, 1954, **96**, 28-35.
28. H. Lee, D. Vashaee, D. Z. Wang, M. S. Dresselhaus, Z. F. Ren and G. Chen, *J. Appl. Phys.*, 2010, **107**, 094308.
29. A. F. Ioffe, *Semiconductor Thermoelements and Thermoelectric Cooling*, Infosearch, London, 1957.
30. G. A. Slack and M. A. Hussain, *J. Appl. Phys.*, 1991, **70**, 2694.
31. Z. Wang, J. E. Alaniz, W. Jang, J. E. Garay and C. Dames, *Nano Lett.*, 2011, **11**, 2206.
32. T. C. Bor, A. T. W. Kempen, F. D. Tichelaar, E. J. Mittemeijer and E. V. D. Giessen, *Philos. Mag. A*, 2002, **82**, 971.
33. M. F. Ashby and L. M. Brown, *Philos. Mag.*, 1963, **8**, 1649.
34. M. F. Ashby and L. M. Brown, *Philos. Mag.*, 1963, **8**, 1083.
35. A. Armigliato and P. Werner, *Ultramicroscopy*, 1984, **15**, 61.
36. A. Armigliato, A. Parisini, R. Hillebrand and P. Werner, *Phys. stat. sol.* (a), 1985, **90**, 115.
37. P. D. Desai, *J. Phys. Chem. ref. data*, 1986, **15**, 967.